

MCNPX Estimation of Photoneutron Dose to Eye Voxel Anthropomorphic Phantom From 18 MV Linear Accelerator

Dose-Response:
An International Journal
April-June 2023:1-7
© The Author(s) 2023
Article reuse guidelines:
sagepub.com/journals-permissions
DOI: 10.1177/15593258231169807
journals.sagepub.com/home/dos


Ali AA Alghamdi¹ 

Abstract

The dose due to photoneutron contamination outside the field of irradiation can be significant when using high-energy linear accelerators. The eye is a radiation-sensitive organ, and this risk increases when high linear energy transfer neutron radiation is involved. This study aimed to provide a fast method to estimate photoneutron dose to the eye during radiotherapy. A typical high-energy linear accelerator operating at 18 MV was simulated using the Monte Carlo N-Particle Transport Code System extended version (MCNPX 2.5.0). The latest International Atomic Energy Agency photonuclear data library release was integrated into the code, accounting for the most known elements and isotopes used in typical linear accelerator construction. The photoneutron flux from a $5 \times 5 \text{ cm}^2$ field size was scored at the treatment table plane and used as a new source for estimating the absorbed dose in a high-resolution eye voxel anthropomorphic phantom. In addition, common shielding media were tested to reduce the photoneutron dose to the eye using common shielding materials. Introducing a 2 cm thickness of common neutron shielding medium reduced the total dose received in the eye voxel anthropomorphic phantom by 54%. In conclusion, individualized treatment based on photoneutron dose assessment is essential to better estimate the secondary dose inside or outside the field of irradiation.

Keywords

photoneutron dose, eye model, voxel anthropomorphic phantom, weight window

Introduction

The use of high-energy photon beams for deep-seated tumors has several advantages. However, assessment of associated secondary photoneutron contamination is also essential for complete patient dose profiling. The neutron fluence behavior and energy spectra are difficult to measure directly. Therefore, recommendations¹⁻³ covering photonuclear cross-section data and the best methods for neutron measurements in a high-energy radiotherapy suite have been issued. Several important parameters must be considered for photoneutron dose investigation during radiotherapy, including complete specifications for the linear accelerator and full knowledge of the elemental compositions of all materials inside a typical radiotherapy treatment room.^{2,3} However, there are few studies on short-lived⁴ or long-lived isotopes produced by photonuclear or photoneutron products.⁵ The Monte Carlo (MC) simulation is one of the most effective tools for assessing

photoneutron doses. A total of 71% of relevant studies have utilized MC methods, and all experimental works are accompanied by analytical or MC calculations. In addition, MC is the preferred choice for improving the calculation time (owing to increased computational capacity) and the availability of photonuclear cross-section data.⁶

The majority of photoneutrons are produced by heavy elements (tungsten (W), lead (Pb), copper (Cu), and iron (Fe))

¹ Department of Radiological Sciences, College of Applied Medical Science, Imam Abdulrahman Bin Faisal University, Dammam, Saudi Arabia

Received 3 August 2022; accepted 27 March 2023

Corresponding Author:

Ali AA Alghamdi, Department of Radiological Sciences, College of Applied Medical Science, Imam Abdulrahman Bin Faisal University, P.O. Box 2435, Dammam, Saudi Arabia 31441.
Email: alalghamdi@iau.edu.sa



Creative Commons Non Commercial CC BY-NC: This article is distributed under the terms of the Creative Commons Attribution-NonCommercial 4.0 License (<https://creativecommons.org/licenses/by-nc/4.0/>) which permits non-commercial use, reproduction and distribution of the work without further permission provided the original work is attributed as specified on the SAGE

and Open Access pages (<https://us.sagepub.com/en-us/nam/open-access-at-sage>).

in the target and gantry, including beam conforming and shielding compartments.⁷ Multiple bremsstrahlung photons are typically produced by incident electrons. At this stage, there is a negligible probability that neutrons will be produced owing to electron interaction. However, emissions of multiple photoneutrons are possible, depending on the incident photon energy. Different (γ , xn) interactions have different thresholds. In this study, only the (γ , n) interactions are relevant. In most cases, short-lived proton-rich isotopes are produced, particularly from organic elements such as carbon (C), oxygen (O), and nitrogen (N). These isotopes then decay via positron emissions and subsequent gamma emissions. Meanwhile, neutron production involves a typical neutron fission spectrum with an asymmetrical gaseous distribution. Some neutrons are attenuated in the shielding compartments, while some travel isotropically around the treatment room and are scattered, thermalized, and finally absorbed. Various short- and long-lived isotopes can be produced, depending on the absorbing material and neutron energy.⁸

The eye is a high-risk organ during radiation exposure,⁹ and this risk increases when high LET neutron radiation is involved. A previous study investigated the correlation between eye complications and a dose received by head and neck radiotherapy in cases where the eye was on the beam entrance or exit and not the main target for radiotherapy treatment.¹⁰ The photoneutron dose to the eyes outside the irradiation field during radiotherapy treatment was also estimated for a mathematical medical internal radiation dosimetry (MIRD) anthropomorphic phantom¹¹ and for a voxel anthropomorphic phantom.¹² Kim and Lee reported variations in photoneutron production per irradiation field size, indicating that a $20 \times 20 \text{ cm}^2$ irradiation field contributed to a higher photoneutron dose than did other field sizes.¹³ Meanwhile, Dowlatabadi et al. reported a lower photoneutron dose for $20 \times 20 \text{ cm}^2$ and $5 \times 5 \text{ cm}^2$ than for $10 \times 10 \text{ cm}^2$ irradiation field sizes.¹⁴ Taylor and Kron reported fluctuating uncertainties associated with secondary photoneutron dose assessment for photon energies as low as 6 MV, with a comparable risk of secondary cancer when using intensity-modulated radiation therapy (IMRT) at 18 MV photon energy.⁶ Therefore, radiation-sensitive organs outside the field of irradiation can be exposed to additional photoneutron doses.¹⁵

This study aimed to provide a fast method to estimate photoneutron dose to the eye outside the field of irradiation during radiotherapy treatment. Toward this goal, a simulation of an 18 MV high-energy linear accelerator and a high-resolution eye voxel anthropomorphic phantom was carried out using MCNPX 2.5.0¹⁶ to estimate the photoneutron dose to the eye at a peripheral position ($X = 0$, $Y = 20$ and $Z = -100 \text{ cm}$) from a $5 \times 5 \text{ cm}^2$ irradiation isocenter field size.

Materials and Methods

The simulation scenario accounted for most of the major structures found in a typical medical linear accelerator operating at 18 MV energy with a $5 \times 5 \text{ cm}^2$ irradiation isocenter

field size. The dimensions of the linear accelerator were determined as previously described.¹⁷ In addition, primary shielding, and iron shielding of the multileaf collimator (MLC) were included. The simulation consisted of 2 stages. First, photoneutrons were tracked from their origin in the target, flattening filter, collimation structures, and MLC to a thin disc ($r = 2.5 \text{ cm}$) located on the treatment table plane. The disc was located in air at an approximate position from the irradiation field of the beam ($X = 0$, $Y = 20$, and $Z = -100$). This closely resembled a normal position where the patient was lying supine, and the disc was positioned on top of the open-eye voxel anthropomorphic phantom. The F4 tally was a volume-based tally that used the entire disc, and the upper and lower surfaces of the disc were used with the F1 surface tally to compare and crosscheck the photoneutron-scored spectra. The tallied flux energy bins were used to describe a disc of the same size as the new photoneutron source. The tallied photoneutron spectra across the disk were used as the photoneutron source in the second stage of the simulation. The new source was positioned in an eye anthropomorphic voxel phantom to simulate photoneutron dose deposition. In addition, the photoneutron flux was tallied independently across the table plane (-100 to 100 cm) using the F5 detector tally.

Most eye dosimetry models were employed for radiation treatment planning and dose conversion factor calculation.^{15,18} The voxel eye anthropomorphic phantom¹⁹ employed in this study was based on 81 slices obtained from the female data of the Visible Human project. Semi-auto segmentation was carried out by color labeling each pixel. Consequently, 15 identified structures were assigned 15 identification (ID) numbers, and the entire phantom was adapted into MCNPX using a lattice card.¹⁸ The data were presented as a $256 \times 256 \times 81$ with a voxel size of $.33 \text{ mm}^3$. Each slice was segmented with different color intensities to contrast various organs/tissues in the original images. Figure 1 shows part of the geometry of the simulated linear accelerator treatment head specifying a $5 \times 5 \text{ cm}^2$ irradiation field size and the geometry section of the open-eye voxel anthropomorphic phantom using MCNPX plotting, featuring color intensities for various tissue volumes identified in the phantom. The shielding thickness suggested for the photoneutron is shown at the top of the phantom and explained further in the Results section.

The latest photonuclear data libraries were downloaded from the IAEA portal.¹ The data included details of cross-sections and the accompanying emission spectra for 209 isotopes in the evaluated nuclear data file format suitable for MCNPX processing. The integration was completed by inserting all element array file headings into an MCNPX cross-section directory (xdir) array list and the full library into an MCNPX library directory. Thus, defining the photonuclear library with an extension photonuclear designation (0000.12u) following each element isotope for the material card in the MCNPX input file.

To increase the precision of the MC calculations, a group of techniques referred to as variance reduction methods were adopted to improve the efficiency of the simulation. A mesh-superimposed importance weight-window generator was used for variance

reduction in the simulation. A rectangular mesh was tested, and the best combination for setting the window boundaries along the Z-plane of the beam with 2 large bins (X- and Y-planes) covering the entire geometry was determined. The window boundaries along the Z-direction were varied and increased in the region of scoring interest parallel to the assumed plane of the treatment table, where the F5 detector tally and F4 flux tally were located.

The total energy deposition tally (+F6) was used to score the dose in each tissue identified in the eye voxel anthropomorphic phantom. Additional mesh tallies were set independently from the previous mesh to investigate the efficiency problems of the source, photoneutron flux, and photoneutron flux across the geometry. Several cards necessary for the run were activated in the MCNPX file. The bremsstrahlung basing card was used to improve bremsstrahlung production. Physics cards for electrons, photons, and neutrons were used to control the upper- and lower-energy limits. A photonuclear material card and force collision cards for photons and neutrons were used to define materials for photonuclear table interaction and forcing of neutron or photon collisions in each cell.

The compartment structures and elemental compositions employed in the simulations of the gantry head of the linear

accelerator are listed in Table 1. The amount of each isotope was included as the abundance fraction of natural elements when available in the new photonuclear library. A voxel eye anthropomorphic phantom was used to identify the tissues, and elemental compositions were adopted.¹⁹ The computer used for the simulation was a Hewlett-Packard Pavilion Laptop AMD Ryzen 7, with a frequency of 1801 Mhz.

Results

The weight-window boundaries were fitted to avoid overlapping cell boundary planes. Figure 2 illustrates the tracked photoneutrons across the problem geometry in a thin slice of fine mesh of $1 \times 1000 \times 1000$ bins along the x-, y-, and z-planes. The image illustrates the effect of using a mesh-based weight-window generator. The number of generated neutrons were checked in the MCNPX print table for neutron particle creation against the lost neutron particles for boundary optimization. The number of neutrons and the efficiency (number of particles/computer time) of the source were 10× higher with the weight-window methods than that with the no variance reduction method. The design of the mesh was

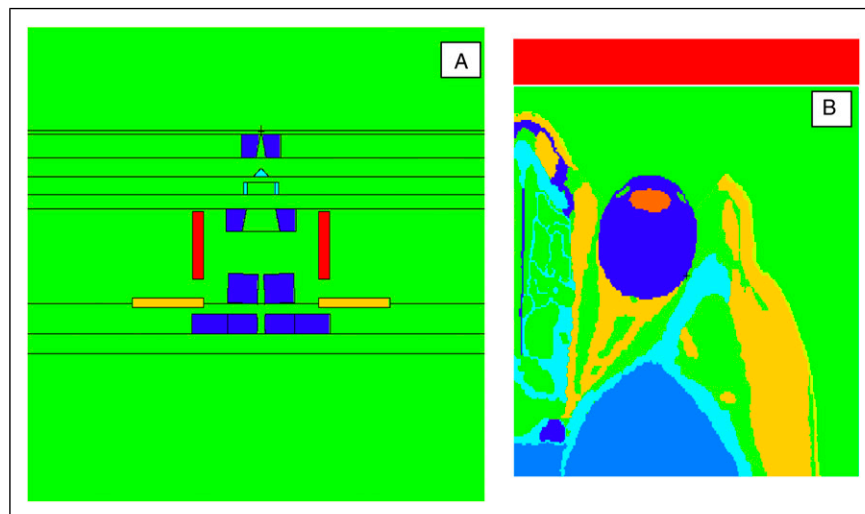


Figure 1. (A) ZX plane cross-section of the linear accelerator treatment head showing the main simulated structures. (B) ZY plane cross-section of the eye anthropomorphic phantom showing the identified tissues and organs. The shielding thickness suggested for the photoneutron is shown on the top of the phantom. Note that the dimension is not to scale.

Table 1. Linear Accelerator Main Structures and Elemental Compositions Included in the Simulation.

Linear Accelerator Compartment	Elemental Composition	Isotopes	Density (g/cm ³)
Target, primary collimator, secondary collimator, upper and lower jaws, and MLC	W	W180, W182, W183, W184, W186	18
Gantry shielding	Pb	Pb206, Pb207, Pb208	11.4
MLC shielding	Fe	Fe54, Fe56, Fe57, Fe58	7.87
Target filter, flattening filter, and ionization chamber casing	Cu	Cu63, Cu65	8.93
Air	C, O, N	C12, C13, O16, O17, N14, N15	1.23×10^{-3}

orientated to the scoring position, resulting in more particles being generated toward the region and the tally of interest. Detailed discussions of weight-window settings include several options.^{20,21} The simulation files were run, on average, a 3×10^8 particle history until satisfactory statistical and MCNPX code limits checks were achieved, with a maximum reported relative error of less than 1%. The computer time

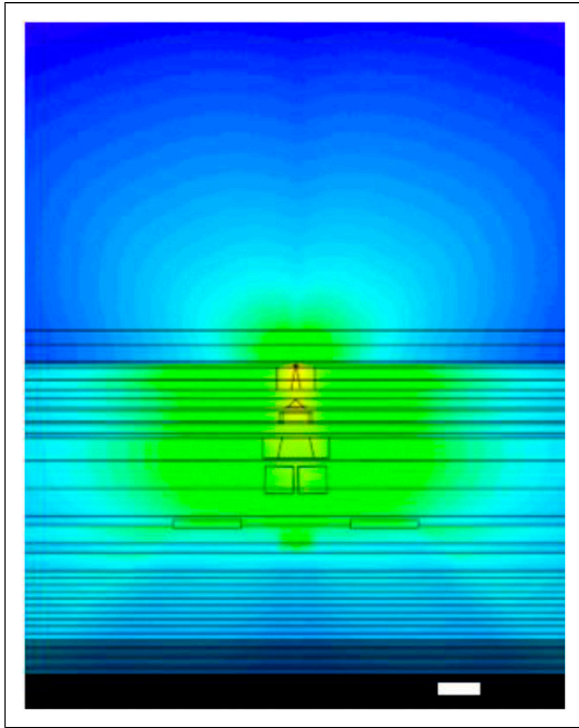


Figure 2. Tracked photoneutrons/source particles across z and y , superimposed over the linear accelerator geometry. The lines of the mesh-based weight-window generator align and vary toward the region of interest at the table plane. The disc place shown schematically out of the scale to the corner of the figure.

varied with the tally type, with a maximum time of (260 min) to score the average photoneutron spectrum using the F4 tally.

The F5 detector diagnostic tally was designed as a selected sized detector sphere ($r = 5$ cm in this study) with defined coordinates along the plane of the table (from the isocenter -100 cm to the 100 cm Y -plane (Figure 3)). As the name implied, F5 provided diagnostic information regarding the contribution of photoneutrons from different parts of the geometry. This information was printed as a table, along with the results of the tally. It showed the photoneutron generation in each cell defined in the geometry and contributed to F5 tally detection spheres. The analysis of these results indicated that the contribution of the major structures varied with the location of the detection sphere. In general, the main contributions were from the primary collimator, flattening filter, target, secondary collimator, upper and lower jaws, and MLC. The photoneutron flux inside the beam was slightly less than 20 cm outside the field of irradiation and then dropped gradually with increasing distance from the isocenter.

The F4 tally of the photoneutron flux from the irradiation field is shown in Figure 4. Ideally, a source surface file could be created; however, the distal position of the tallied surface and accumulation of sufficient particles to create a source file could exceed the capacity of the computer used in this study. Thus, a simpler source was assumed by obtaining as much information as possible (i.e., energy and spectral direction). The energy and direction of the new source were defined using an SDEF source card. The new source direction assumed equal emission probability and was perpendicular to the open-eye voxel anthropomorphic phantom, with energy bin intensities provided by F4 tally.

The results of the dose calculations in major tissues and organs identified in the eye voxel anthropomorphic phantom are listed in Table 2. The results from the F6 tally were obtained in MeV/Gram and then converted to absorbed dose using a tally multiplier with an appropriate unit conversion factor ($C = 2.6 \times 10^{-8}$) to Rad/Gram. The total dose to the eye was reported in SV/hr/source particles

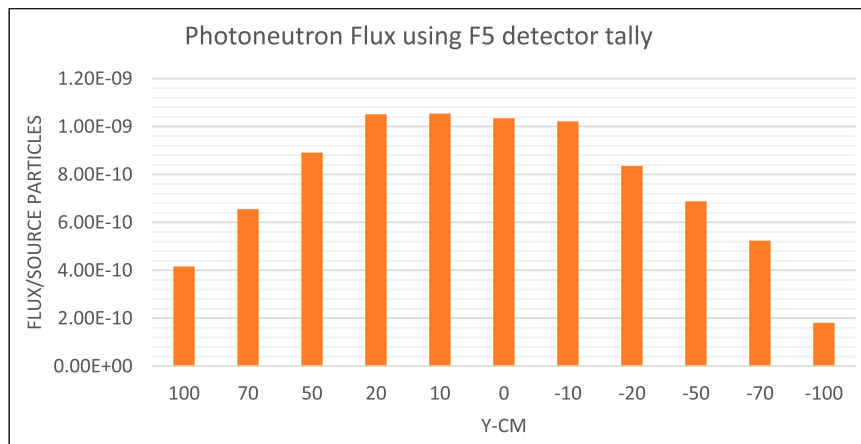


Figure 3. Photoneutron flux scored across the table plane using the F5 diagnostic detector tally.

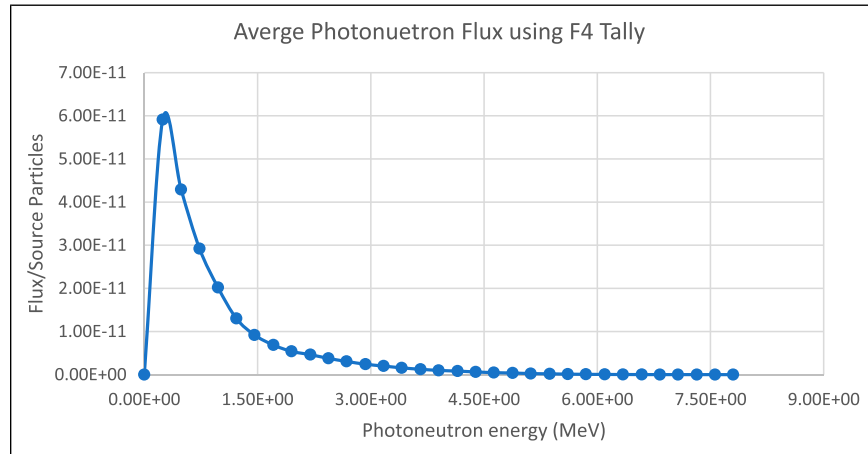


Figure 4. Average flux tallied using the F4 tally at a disc cell located $x = 0$, $y = 20$ and $z = -100$ cm from the isocenter.

Table 2. Dose ($\mu\text{Gy}/\text{Number Particle History}/\text{MU}$) Scores in Major Tissues and Organs Identified in the Eye Voxel Anthropomorphic Phantom and the Effect of Introducing 2 cm Shielding Thickness of Polycarbonate and Water.

Tissue/Organ	No Shielding μGy	Polycarbonate μGy	%	Water μGy	%
Bone	2.57×10^{-5}	1.18×10^{-5}	-54	1.47×10^{-5}	-42.7
Brain	4.41×10^{-5}	1.90×10^{-5}	-57	2.42×10^{-5}	-45
Fat	6.46×10^{-5}	2.78×10^{-5}	-56.9	3.51×10^{-5}	-45.7
Muscle	3.45×10^{-5}	1.47×10^{-5}	-57.5	1.86×10^{-5}	-46
Ligament	4.90×10^{-7}	2.36×10^{-7}	-51.8	2.92×10^{-7}	-40
Cornea	6.37×10^{-4}	3.37×10^{-4}	-47	4.08×10^{-4}	-36
Eye gel	5.78×10^{-3}	2.45×10^{-3}	-57	3.11×10^{-3}	-46
Lens	4.90×10^{-6}	2.55×10^{-6}	-48	3.09×10^{-6}	-37
Optic nerve	7.28×10^{-5}	2.96×10^{-5}	-59	3.80×10^{-5}	-47
Sclera	1.97×10^{-4}	7.99×10^{-5}	-59	1.03×10^{-4}	-48
Epidermis	8.67×10^{-5}	3.91×10^{-5}	-55	4.86×10^{-5}	-44
Lacrimal gland	1.83×10^{-5}	9.68×10^{-6}	-47	1.16×10^{-5}	-36
Soft tissues	5.01×10^{-4}	3.70×10^{-4}	-26	4.30×10^{-4}	-14
Total	7.47×10^{-3}	3.39×10^{-3}	-54.6	4.25×10^{-3}	-43.1

using a built-in dose function in conjunction with a + F6 tally.¹⁶

Discussion

Radiation-sensitive organs outside the field of irradiation, such as the eyes, can be exposed to additional photoneutron doses. In this study, the total absorbed dose for all the tissues and organs identified in the eye anthropomorphic voxel phantom was $0.00473 \mu\text{Gy}/\text{source particle}/\text{MU}$, and the total equivalent dose was $4.443 \times 10^{-9} \text{SV}/\text{hr}/\text{source particle}$. Studies such as Martinez-Ovalle et al. and Chegeni et al.^{11,12} on the photoneutron dose to the eye outside the field of irradiation for a typical 18-MeV photon beam radiotherapy treatment reported larger doses. In a voxel anthropomorphic model for adult patients, the total absorbed dose was $1.9 \mu\text{Gy}$ in the eye lens, eye gel, and optic nerve from anterior-posterior pelvic

treatment of $24.6 \times 17.7 \text{cm}^2$ irradiation field. The eye lens in a voxel anthropomorphic model for an adult patient recorded an absorbed dose of $1.05 \mu\text{Gy}$, higher than that in other eye tissues. In the study Martinez-Ovalle et al.,¹¹ the status of the segmented eyelid was unclear for the voxel anthropomorphic phantom version (ie, how much of the lid covered the eye). This may suggest that photoneutrons were absorbed on the eyelid and explain the lower dose to the eye gel, where most of the photoneutron dose is expected. A mathematical MIRD anthropomorphic phantom¹² reported the highest total absorbed dose of $.0531 \text{mGy}$ and equivalent dose of $.983 \text{mSV}$, estimated from a $10 \times 10 \text{cm}^2$ irradiation field for the anterior-posterior beam in the abdominal region. The dose reported to the eyes in these studies referred to both eyes. Meanwhile, in the study Chegeni et al.,¹² the eyelid was not included in the MIRD anthropomorphic phantom study and was segmented out for the open-eye model in the current study. The

discrepancies between the results can be attributed to the differences in eye models, field sizes, scoring positions, and linear accelerator specifications. Despite these differences, the overall results indicate the significance of the secondary photoneutron dose on peripheral sensitive organs, such as the eye, regardless of the field size.

Dose deposition is more common in the eye gel because it constitutes the largest tissue in the eye and provides a perfect watery medium for scattering and absorbing photoneutrons. Table 2 provides a comparison of the dose calculated in major tissues along with the effect of introducing a 2 cm thickness neutron shielding media (polycarbonate²² and water). Introducing a material with a higher concentration of hydrogen (H) attenuates a large portion of the photoneutron fission spectrum. Water also reduces the total dose received by the sensitive eye tissues by 43%, while polycarbonate reduces the dose by an average of 50%. This ratio can be increased by properly refining the protective thickness. New materials with suitable shielding properties for both fast and thermal neutrons are under investigation,^{23,24} with initial reports indicating more than 70% efficiency. Applying the necessary protection when the oncology team decides on the course of treatment is a routine practice in radiation therapy. However, few innovative practices have been suggested^{25,26} for cases in which photoneutron dose assessment is fully conducted.

Many studies have discussed inherent limitations in photoneutron dose estimation,^{27–30} including the underestimation of MC simulations for photoneutron spectra under 1 MeV and other factors affecting analytical calculations, MC calculations, and experimental measurements of optimal conditions for photoneutron dose assessment. The simplified photoneutron source used in this study may lead to underestimation of the photoneutron dose. Photoneutron components, which originate from within the patient or from other materials not included in the simulation, affect the amount and position of photoneutron production and, eventually, the expected photoneutron dose. A total of 14 major structures were simulated in this study, which covers the major structures from the point where the electron beam interacts with the target onward to the isocenter. Other structures require detailed manufacturer specifications, which normally include the geometrical layout and, importantly, the elemental composition of each material. Photoneutron production depends on the energy and elemental photonuclear cross-section; therefore, full knowledge of these details is required for better estimation of the photoneutron dose.

Conclusion

The eye voxel anthropomorphic phantom provides a fast method for photoneutron dose assessment in specific cases. The general principle of radiation protection requires that unwanted radiation should be diminished and that patients should receive minimal unnecessary extra doses. Therefore, individual photoneutron dose assessment is essential to better approximate the secondary dose for complete patient dose

profiling. A small eyelid thickness may contribute significantly to the dose received in the eye gel. Suitable shielding with moderate protection reduces the received dose to the peripheral radiation-sensitive organs.

Declaration of Conflicting Interests

The author(s) declared no potential conflicts of interest with respect to the research, authorship, and/or publication of this article.

Funding

The author(s) received no financial support for the research, authorship, and/or publication of this article.

Data Availability

The data for the voxel eye anthropomorphic phantom used in this study are available from the corresponding author on reasonable request.

ORCID iD

Ali AA Alghamdi  <https://orcid.org/0000-0003-4568-7144>

References

1. International Atomic Energy Agency (IAEA) [Internet]. IAEA Evaluated Photonuclear Data Library (IAEA/PD-2019). <https://www-nds.iaea.org/photonuclear/> Cited January 18, 2022.
2. NCRP REPORT No. 79. *Neutron Contamination from Medical Electron Accelerators*. 79. NCRP; 1984.
3. American Association of Physicist in Medicine (AAPM). *Report No 19: Neutron Measurements Around High Energy X-Ray Radiotherapy Machines*. AAPM; 1986.
4. Alghamdi AA, Al-Mokhlef J, Alhaj A, Spyrou NM. Feasibility study of using PET to determine nitrogen concentration after high energy photon irradiation. *J Radioanal Nucl Chem*. 2007;271(3):783-787.
5. Kwon NH, Shin DO, Kim J, et al. Current status of disposal and measurement analysis of radioactive components in linear accelerators in Korea. *Nucl Eng Technol*. 2022;54(2):507-513.
6. Taylor ML, Kron T. Consideration of the radiation dose delivered away from the treatment field to patients in radiotherapy. *J Med Phys*. 2011;36(2):59-71.
7. Naseri A, Mesbahi A. A review on photoneutrons characteristics in radiation therapy with high-energy photon beams. *Rep Practical Oncol Radiother*. 2010;15(5):138-144.
8. Fischer HW, Tabot B, Poppe B. Comparison of activation products and induced dose rates in different high-energy medical linear accelerators. *Health Phys*. 2008;94(3):272-278.
9. Authors on behalf of ICRP; Stewart FA, Akleyev AV, Hauer-Jensen M, et al. ICRP publication 118: ICRP statement on tissue reactions and early and late effects of radiation in normal tissues and organs—threshold doses for tissue reactions in a radiation protection context. *Ann ICRP*. 2012;41(1-2):1-322.
10. Nuzzi R, Trossarello M, Bartoncini S, et al. Ocular complications after radiation therapy: An observational study. *Clin Ophthalmol*. 2020;14:3153-3166.

11. Martinez-Ovalle SA, Barquero R, Gomez-Ros JM, Lallena AM. Neutron dosimetry in organs of an adult human phantom using linacs with multileaf collimator in radiotherapy treatments. *Med Phys*. 2012;39(5):2854-2866.
12. Chegeni N, Karimi AH, Jabbari I, Arvandi S. Photoneutron dose estimation in GRID therapy using an anthropomorphic phantom: A Monte Carlo study. *J Med Signals Sens*. 2018;8(3):175-183.
13. Kim HS, Lee JK. Assessment and measurement of the photoneutron field produced in the Varian medical linear accelerator. *J Nucl Sci Technol*. 2007;44(1):95-101.
14. Dowlatabadi H, Mowlavi AA, Ghorbani M, Mohammadi S, Knaup C. Study of photoneutron production for the 18 MV photon beam of the Siemens medical linac by Monte Carlo simulation. *J Biomed Phys Eng*. 2020;10(6):679-690.
15. Bolch WE, Dietze G, Petoussi-Hens N, Zankl M. Dosimetric models of the eye and lens of the eye and their use in assessing dose coefficients for ocular exposures. *Ann ICRP*. 2015;44(1 suppl 1):91-111.
16. Pelowitz DB. *MCNPXTM User's Manual, Version 2.5.0*. Santa Fe, NM: Los Alamos National Laboratory; 2005.
17. Ma A, Awotwi-Pratt J, Alghamdi A, Alfuraih A, Spyrou NM. Monte Carlo study of photoneutron production in the Varian Clinac 2100C linac. *J Radioanal Nucl Chem*. 2008;276(1):119-123.
18. De Maria C, Iorio S, Montemurro F, et al.. Phantoms in medicine: The case of ophthalmology. *Biomed Sci Eng* 2019;3(1):61-69.
19. Alghamdi AA, Ma A, Marouli M, Albarakati Y, Kacperek A, Spyrou NM. A high-resolution anthropomorphic voxel-based tomographic phantom for proton therapy of the eye. *Phys Med Biol*. 2007;52(2):N51-N59.
20. Hendricks JS, Culbertson CN. *An Assessment of MCNP Weight Windows*; 2000.
21. Hoogenboom JE, Légrády D. A critical review of the weight window generator in MCNP. Proc. Monte Carlo 2005 Topical Meeting: The Monte Carlo Method–Versatility Unbounded in a Dynamic Computing World; Chattanooga, TN; April 17-21, 2005.
22. Gaylan Y, Bozkurt A, Barış AV. Investigating thermal and fast neutron shielding properties of B₄C, B₂O₃, Sm₂O₃, and Gd₂O₃ doped polymer matrix composites using Monte Carlo simulations. *Süleyman Demirel Üniversitesi Fen Edebiyat Fakültesi Fen Dergisi*. 2021;16(2):490-499.
23. Tuna T, Eker AA, Kam E. Neutron shielding characteristics of polymer composites with boron carbide. *J Kor Phys Soc*. 2021;78(7):566-573.
24. Woosley S, Abuali Galehdari N, Kelkar A, Aravamudhan S. Fused deposition modeling 3D printing of boron nitride composites for neutron radiation shielding. *J Mater Res*. 2018;33(22):3657-3664.
25. Khabaz R, Zanganeh V. A feasibility study to reduce the contamination of photoneutrons and photons in organs/tissues during radiotherapy. *iran J Medical Phys*. 2020;17(6):366-373.
26. Kakino R, Nakamura M, Hu N, et al. Photoneutron-induced damage reduction for cardiac implantable electronic devices using neutron-shielding sheets in high-energy X-ray radiotherapy: A phantom study. *Phys Med*. 2021;89:151-159.
27. Vega-Carrillo HR, Martinez-Ovalle SA, Lallena AM, Mercado GA, Benites-Rengifo JL. Neutron and photon spectra in LINACs. *Appl Radiat Isot*. 2012;71:75-80.
28. Karimi AH, Brkić H, Shahbazi-Gahrouei D, Haghghi SB, Jabbari I. Essential considerations for accurate evaluation of photoneutron contamination in radiotherapy. *Appl Radiat Isot*. 2019;145:24-31.
29. Beigi M, Afarande F, Ghiasi H. Safe bunker designing for the 18 MV varian 2100 Clinac: a comparison between Monte Carlo simulation based upon data and new protocol recommendations. *Rep Practical Oncol Radiother*. 2016;21(1):42-49.
30. Ashrafinia M, Hadadi A, Sardari D, Saeedzadeh E. Investigation of LINAC structural effects on photoneutron specified parameters using FLUKA code. *Iran J Medical Phys*. 2020;17(1):7-14.